

Investigation of the opto-magnetic properties of Co doped ZnO nanoparticles and thin films for spintronics

E. M. M. Ibrahim^a, A. Z. Mahmoud^{b,c}, L. Galal^{b,d}, Y. El Sayed^{e,f},
E. R. Shaaban^{g,*}

^aPhysics Department, Faculty of Science, Sohag University, Sohag-82524, Egypt.

^bPhysics Department, Faculty of Science, Assiut University, Assiut, Egypt.

^cPhysics Department, College of Sciences and Art At ArRass, Qassim University, ArRass 51921, Kingdom of Saudi Arabia.

^dPhysics Department, Faculty of Science, Northern Border University, Arar 91431, Saudi Arabia.

^ePhysics Department, Faculty of Sciences, King Khalid University, P. O. Box 9004, Abha, Saudi Arabia.

^fResearch Center for Advanced Materials Science (RCAMS), King Khalid University, Abha 61413, P. O. Box 9004, Saudi Arabia.

^gPhysics Department, Faculty of Science, Al-Azhar University, Assiut, 71542, Egypt.

Zn_{1-x}Co_xO (0 ≤ x ≤ 0.10) nanocrystalline compounds with different compositions were prepared by ball milling, and thin films of these compounds were prepared by electron evaporation method. XRD patterns are used to study the structural properties of these films. All films showed a hexagonal wurtzite structure. Using XRD patterns, calculate crystallite. The optical constants *n* and *k* of the Zn_{1-x}Co_xO nanocrystalline film are calculated in the range of 300-2500 nm based on K-K method. As Co is more doped, the refractive index also shows an increase. According to the Tauc relationship, the optical energy gap of the Zn_{1-x}Co_xO film is calculated, which proves to be a direct transition.

(Received August 26, 2021; Accepted November 12, 2021)

Keywords: Zn_{1-x}Co_xO thin films, Zinc blend wurtzite, Spectrophotometer: K-K method, Optical constants, Energy gap, Hysteresis loop

1. Introduction

Unlike non-oxide semiconductors, oxide semiconductors are known to have a wide band gap energy greater than 3.0 eV. With such a large semiconductor band gap, they are optically transparent in the visible light region and are suitable for short-wavelength light applications. The most common examples of such oxide semiconductors are ZnO, TiO₂, SnO₂, In₂O₃, etc. [1]. Diluted magnetic semiconductors (DMS) and special transition metal doped semiconductors with a Curie temperature equal to or higher than room temperature ferromagnetism (RTFM) have recently attracted widespread interest due to their importance in spintronics and magneto-optical applications [2-4]. They are also the main candidates for various multifunctional applications, such as solar cells, sensors, liquid crystal displays (LCD) and transparent electronics. After adding spin function, they can be used to produce spin LEDs, spin FET and magnetic memory [5-7]. Therefore, it can provide optoelectronics for a new generation of spintronic devices. The transmitted ferromagnetic DMS can be achieved by doping transition metal (TM) ions into wide band gap semiconductors, sea cations [8, 9], especially zinc oxide, with wide band gap (3.3 eV) and high exciton binding energy (60 meV).) Extracted from ZnO [10]. ZnO has good mechanical properties, is environmentally safe and inexpensive. Therefore, in addition to its potential applications as nanowire lasers, field-effect transistors, nonlinear optical materials, and high-sensitivity chemical sensors, it is also recommended for many ZnO-based DMSs [11] for ferromagnetic prospects above room temperature [12-14]. In the past few years, as reported by Radovanovic [15], Norberg [16] and Ueda [17], TM (Co, Mn, Fe, Ni, Cr) exhibits RT

* Corresponding author: esam_ramadan2008@yahoo.com

ferromagnetism. Therefore, the purpose of this work is to synthesize Co-doped ZnO nanocrystalline films with various doping concentrations by electron beam deposition technology to study the influence of photoelectric and magnetic properties on Co doping in the ZnO main semiconductor matrix. The microstructure and morphological characteristics are also studied.

2. Experimental

Commercial ZnO powder and Co powder with high purity of 99.999%, Sigma Aldrich is used as the starting material. Mix 10% Co powder with ZnO powder respectively according to the following chemical reaction:



After that, a mechanical zirconia ball mill was used to grind the powder at a speed of 350 rpm for (2, 4, 6, 8 and 10hours). To avoid overheating, the mixture was alternately stopped for 10 minutes.

The mixed powder is compressed to make round particles. These $\text{Zn}_{1-x}\text{Co}_x\text{O}$ particles with composition ($x = 0.0, 0.02, 0.04, 0.06, 0.08$ and 0.10) are deposited on the glass substrate by Edward 306 Auto electron beam deposition device with a vacuum of about 10^{-6} Pa. The film thickness and deposition rate are controlled using a quartz crystal FTM6 monitor.

Use an X-ray diffractometer (X-ray diffractometer 6000 from Shimadzu, made in Japan, with CuK_α radiation of $\lambda = 0.15418$ nm) to check the structure of powders and films.

It is well known that energy dispersive X-ray spectroscopy (EDXS) technology can provide precise information about the composition of alloy elements. A scanning electron microscope (SEM) micrograph (JEOL JEM 1230, Japan) model was used to study the morphology of the thin film sample.

The transmittance (T) and reflectance (R) measurements were performed using a double-beam (Shimadzu UV-2101 combined with PC) computer-controlled spectrophotometer, at normal incidence of light and in a wavelength range between 300 and 2500 nm. Refractive index (n) and Extinction coefficient (k) are all extracted by the Kramers-Kronig (K-K) relations using the T and R measured data.

Vibrating sample magnetometer model (VSM-9600M-1, USA) is used to study the magnetic properties of thin films; the maximum applied magnetic field around 17 kOe.

3. Results and discussion

3.1. X-ray diffraction and morphological analysis

Figure 1a shows, the $\text{Zn}_{0.9}\text{Co}_{0.10}\text{O}$ powder was checked according to XRD with different milling time (2, 4, 6, 8 and 10h). On the other hand, the structure of $\text{Zn}_{1-x}\text{Co}_x\text{O}$ ($0 \leq x \leq 0.1$) powder samples was investigated by XRD technique and show in Fig. 1b. The XRD chart shows that polycrystalline structure of the samples. In addition, the crystal structure of pure $\text{Zn}_{1-x}\text{Co}_x\text{O}$ corresponds to the hexagonal wurtzite structure.

The crystal size, D_v , for the $\text{Zn}_{0.9}\text{Co}_{0.1}\text{O}$ and $\text{Zn}_{1-x}\text{Co}_x\text{O}$ are all calculated using the following formula [18, 19]

$$D_v = \frac{k \lambda}{\beta \cos(\theta)} \quad (1)$$

and

$$\varepsilon = \frac{\beta}{4 \tan(\theta)} \quad (2)$$

where θ represents the Bragg angle of the diffraction peak, λ represents the wavelength of $\text{CuK}\alpha$ radiation (1.54 Å), and β is the width of the diffraction peak, which describes the broadening of the peak and is determined according to the formula:

$$\beta = \sqrt{\beta_{obs}^2 - \beta_{std}^2} \quad (3)$$

where β_{obs} is the width of the diffraction peak of the sample and β_{std} is the width of the diffraction peak of the standard (silicon).

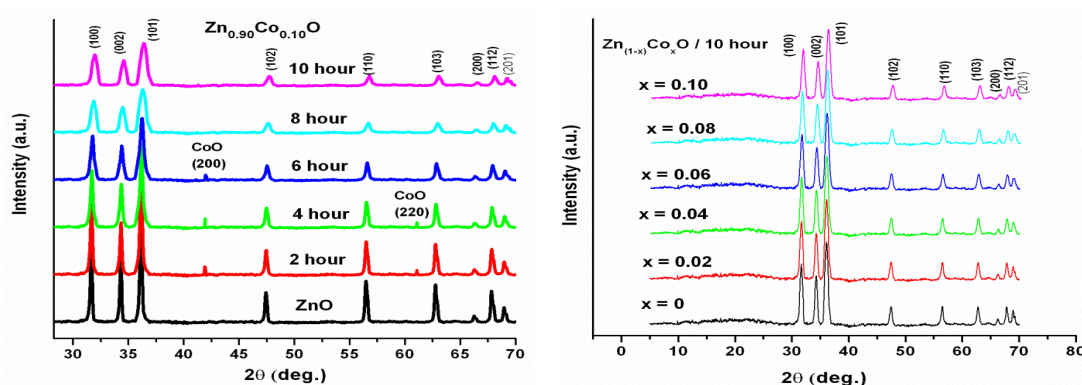


Fig. 1. X-ray diffraction patterns for: a) $\text{Zn}_{0.9}\text{Co}_{0.1}\text{O}$ powder with different milling time. b) $\text{Zn}_{1-x}\text{Co}_x\text{O}$ powder milling for 10h.

Figure 2 shows the D_v , for the $\text{Zn}_{0.9}\text{Co}_{0.1}\text{O}$ with different milling time and $\text{Zn}_{1-x}\text{Co}_x\text{O}$ (where $x = 0, 2, 4, 6, 8$ and 10 at.%). It is found that the crystallite size decreases with the increase of the milling time. Also, at milling time more than 6 h we observed that, D_v are close in size. Furthermore, the smallest size at milling time 10h.

In addition, the crystallite size decreases with increasing Co concentration. Since the addition of Co content in the $\text{Zn}_{1-x}\text{Co}_x\text{O}$ film at the expense of Zn leads to a decrease in grain size and an increase in lattice defects.

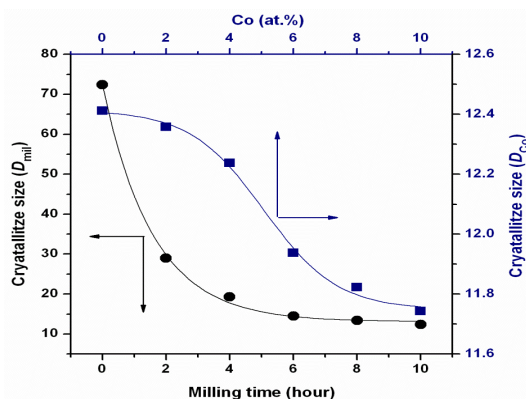


Fig. 2. The variation of D_v with milling time for $\text{Zn}_{0.9}\text{Co}_{0.1}\text{O}$ powder and with Co concentration for $\text{Zn}_{1-x}\text{Co}_x\text{O}$.

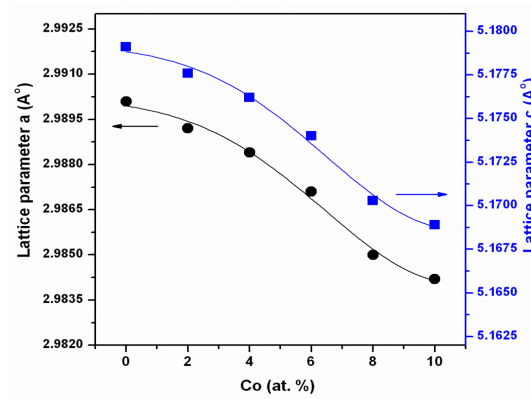


Fig. 3. The lattice constants "a" and "c" with the increasing of Co content for $Zn_{1-x}Co_xO$ film.

The hexagonal wurtzite crystal is characterized by two lattice parameters a and c, and the crystal plane is given by [20, 21]:

$$\frac{1}{d_{hkl}^2} = \frac{4}{3} \frac{h^2 + hk + k^2}{a^2} + \frac{l^2}{c^2} \quad (4)$$

where hkl is the Miller index of the plane. The interplanar distance d_{hkl} of these films is calculated by Bragg's law [16]

$$\lambda = 2d_{hkl} \sin \theta \quad (5)$$

The lattice constants "a" and "c" of the $Zn_{1-x}Co_xO$ film are calculated from the XRD data using the following simple equations:

$$a = b = \lambda (\sqrt{3} \sin \theta)^{-1} \quad (6-a)$$

and

$$c = \lambda (\sin \theta)^{-1} \quad (6-b)$$

Figure 3 show the change of the lattice parameters, a and c, with Co concentration. It is observed that the lattice parameter decreases with the increase of Co content, as the consumption of Zn in the $Zn_{1-x}Co_xO$ film. This behavior has been explained as the radius ion of Co^{+2} (78 pm) is larger than the radius ion of Zn^{2+} (74 pm). Therefore, when Co ions are replaced by Zn ions in the lattice, the lattice parameters "a" and "c" of the $Zn_{1-x}Co_xO$ film compressed.

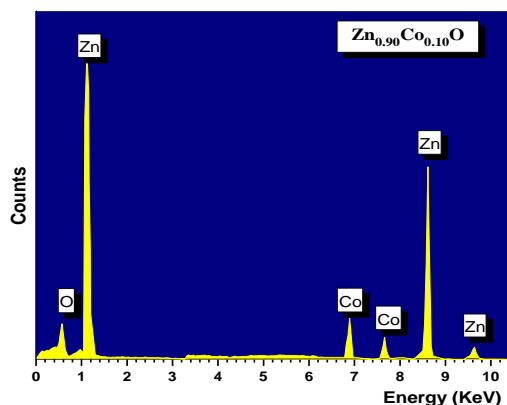


Fig. 4. EDAX spectrum percentage calculated of 10 % Co-doped ZnO thin films.

Figure 5 shows the energy dispersive X-ray spectrum (EDXS) of $Zn_{0.9}Co_{0.1}O$. The spectrum confirmed that there are only three elements, Zn and O, and Co in the Co-doped ZnO film. In addition, EDXS analysis indicated that the composition of all grown films was close to stoichiometric.

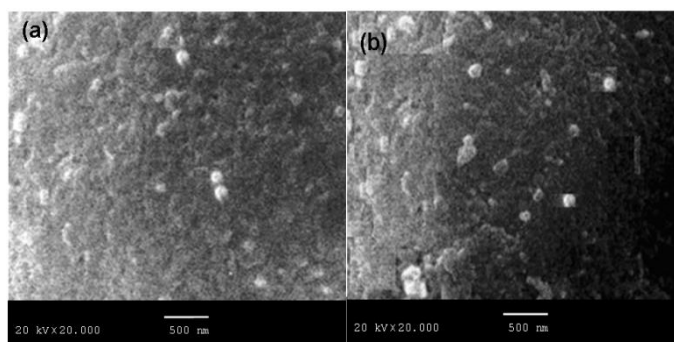


Fig. 5. SEM of nanoparticle of (a) $Zn_{0.92}Co_{0.08}O$ and (b) $Zn_{0.90}Co_{0.10}O$.

3.2. Linear optics of $Zn_{1-x}Co_xO$ nanostructured thin films:

3.2.1. Theoretical background of Kramers-Kronig (K-K) relations

Spectroscopy is undoubtedly one of the best and commonly used procedures for collecting information about the physical properties of thin film materials. However, the type of substrate and growth conditions strongly affects the spectrum, so data analysis is usually not that easy. Therefore, extracting the refractive index n and the extinction coefficient k is very important to understand the optical properties of the studied film [20].

Common procedures for evaluating the complex refractive index ($N' = n + ik$) of films include measuring normal incident reflection (R) and transmission (T) data. However, inferring $N'(\omega)$ from the measured R and T is not easy, and requires an iterative process involving successive approximations to solve the complex rules of R and T based on n and k . In addition, this kind of solution often leads to multiple solutions, and even ends up with a very inaccurate solution. Denton et al. (1972) used $(1-R)/T$ and $(1+R)/T$ instead of R and T to develop a new scheme, ignoring inappropriate results, and slightly modified R , T and film thickness until a reasonable solution is obtained [21]. A method for calculating n and k from the recorded R and T values of normal incidence has been established. This method overcomes the above two problems, namely, no fine-tuning of the measurement data is required and the feasibility of the solution is considered. The method includes the use of iterative procedures to obtain optical constants, the use of successive approximation results of $T(n, k)$ and $R(n, k)$, and the combination of Kramers-Kronig

analysis of the transmitted data to obtain a feasible solution. The Kramers-Kronig dispersion relationship can be used to estimate n and k values from reflectance data, even if the data is only suitable for a narrow spectral range. It does not require any assumptions about the reflectance data beyond the experimental range, or any extrapolation of the data [22-24]. The Kramers-Kronig method is used to calculate the optical constants (n and k) of the $Zn_{1-x}Co_xO$ film based on the reflectance data. N' is given by [25]:

$$N'(\omega) = n(\omega) + ik(\omega), \quad (7)$$

where

$$n(\omega) = \frac{1-R(\omega)}{1+R(\omega)-2\sqrt{R(\omega)}\cos\varphi(\omega)}, \quad (8)$$

$$k(\omega) = \frac{1-R(\omega)\sin\varphi(\omega)}{1+R(\omega)-2\sqrt{R(\omega)}\cos R(\omega)}, \quad (9)$$

and

$$\varphi(\omega) = \frac{-\omega}{\pi} \int_0^{\infty} \frac{\ln R(\omega') - \ln R(\omega)}{\omega'^2 - \omega^2} d\omega', \quad (10)$$

Eq.(10) can be described as:

$$\varphi(\omega_j) = \frac{4\omega_j}{\pi} \times \Delta\omega \times \sum_i \frac{\ln(\sqrt{R(\omega)})}{\omega_i^2 - \omega_j^2}. \quad (11)$$

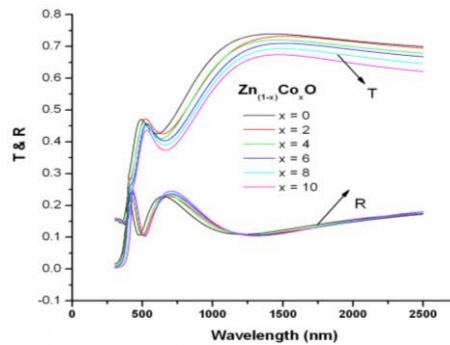


Fig. 6. Transmission, T , and Reflection, R , spectra of $Zn_{1-x}Co_xO$ ($0.0 \leq x \leq 0.10$) thin films.

The spectral behavior of $T(\lambda)$ and $R(\lambda)$ for $Zn_{1-x}Co_xO$ ($0.0 \leq x \leq 0.10$) films are presented in Fig.6. Two transmission edges are seen in the figure around (370 and 450 nm). Here, the first one characterizes as the onset of the absorption edge. Also, an opposite edge can be seen in the figure in the wavelength range 600- 500 nm, which is an optical absorption edge and effectively creates a valley in the transmission spectra between the absorption edge and 1250 nm. The spectra has two prominent regions: (a) the absorption region ($\lambda < 700$ nm) where the sum of $T(\lambda)$ and $R(\lambda)$ is less than unity and (b) the transparent region ($\lambda > 700$ nm) where the film turn into transparent without effective light absorption, $T(\lambda)+R(\lambda) \approx 1$. This is evident from the Fig.6 as well. It can also be seen from the Fig.6 that the amplitude of transmittance decreases while reflectance increases with the Co content in the transparent region. From the figure, the sample exhibit bandpass filter characteristics in the region up to 1250 nm. Part of the light is absorbed in this region and the rest is reflected allowing only a small percentage to pass through.

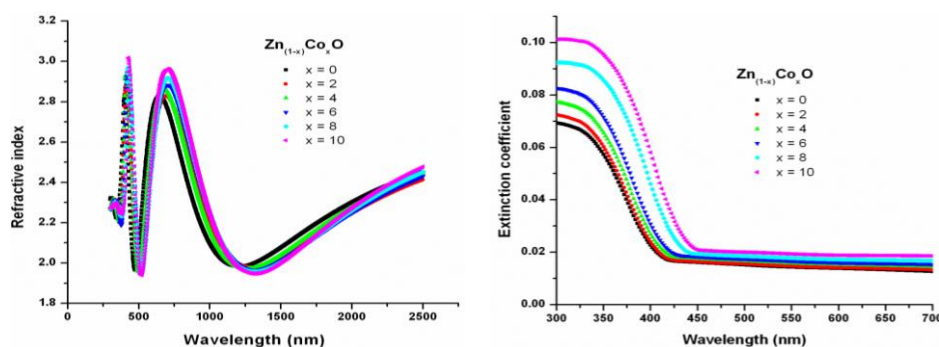


Fig. 7. (a) Refractive index and (b) extinction coefficient, calculated using K-K relations, for different $Zn_{1-x}Co_xO$ ($0.0 \leq x \leq 0.10$) films.

Figures.7(a&b) represent the plots of refractive index and extinction coefficient with respect to the normal incident wavelength, in the range 300 to 2500 nm. The refractive index was calculated from K-K relations. Fig.7(a) shows multiple anomalous and normal dispersion regions in the graph within the range of 300 to 1000 nm and thus exhibits a multi-oscillator model in this range. The anomalous dispersion can be observed in the ranges < 1500 nm while normal dispersion behavior is observed in the ranges 1500- 2500 nm for the as-prepared $Zn_{1-x}Co_xO$ ($0.0 \leq x \leq 0.10$) films. Slight shifts are observed for these ranges with the increasing of the Co content. The anomalous dispersion is due to the coupling of electrons in $Zn_{1-x}Co_xO$ film to the oscillating electric field aroused due to the to the resonance effect of the incident light and the electron polarization [27].

Furthermore, the value of extinction coefficient, k , increases with increasing Co content while it decreases with increasing the wavelength as shown in Fig.7(b). The decrease of k with the wavelength could be attributed to the scattering of light which is responsible for the decrease of the absorption through the doped films. Moreover, k decreases rapidly at short wavelengths (300-450) nm and after that the value of k remains almost constant. The rise and fall in the value of k is directly related to the absorption of light. The lower value of k in the wavelength range > 450 nm implies that these films absorb light in this region very easily [10].

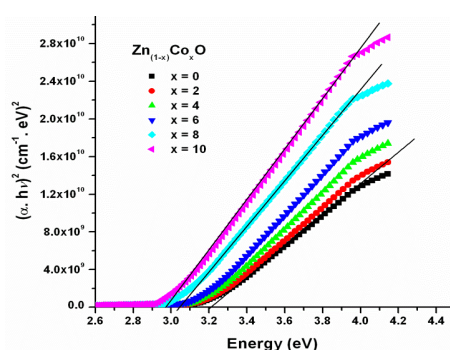


Fig. 8. Tauc's plot for the direct band calculation for $Zn_{1-x}Co_xO$ ($0.0 \leq x \leq 0.10$) films.

Tauc's model is one of the most widely applied techniques to analyze the optical properties of an amorphous material which lets to obtain the band gap energy, E_g , from the coefficient of absorption, α , and energy E . Band gap values of the $Zn_{1-x}Co_xO$ ($0.0 \leq x \leq 0.10$) films was calculated by Tauc's model [28, 29]

$$\alpha h\nu = A(h\nu - E_g)^n, \quad (12)$$

where A is a constant, E_g is the band-gap energy of the material, and n determines the nature of optical transition. For direct allowed transition, $n = 1/2$, for direct forbidden transition, $n = 3/2$, and for indirect allowed transition, $n=2$ [30, 31]. The possible transitions were determined from plots of $(ah\nu)^2$ versus $h\nu$ given in Figure 8. By extrapolating the straight portions of the graphs on $h\nu$ axis, the band-gaps were obtained from the intercepts since $E_g = h\nu$ when $(ah\nu)^2 = 0$. From Fig. 8, it can be seen that the direct band-gap energy values of the $Zn_{1-x}Co_xO$ films decrease from 3.22 eV to 2.96 eV as the Co content increase. This decrease in E_g might be attributed to the decrease the crystallite size and heat of atomization for the composition with increasing the Co content.

Optical conductivity, σ_{opt} , is a convenient tool for analyzing the optical response of a material. This is a generalization of electrical conductivity, σ_{elec} , in the alternating field and is strongly dependent on the electronic states in a material. The electrical and optical conductivity (σ_{elec} and σ_{opt}) can be estimated from the experimental absorption coefficient α , using the relations [32]

$$\sigma_{opt} = \frac{\alpha n c}{4\pi}, \quad (13)$$

and

$$\sigma_{elec} = \frac{2\lambda\sigma_{opt}}{\alpha}, \quad (14)$$

where n is refractive index and c is the velocity of light. Figs.9(a&b) demonstrates the optical and electrical conductivity with respect to the wavelength for the $Zn_{1-x}Co_xO$ ($0.0 \leq x \leq 0.10$) as-prepared films.

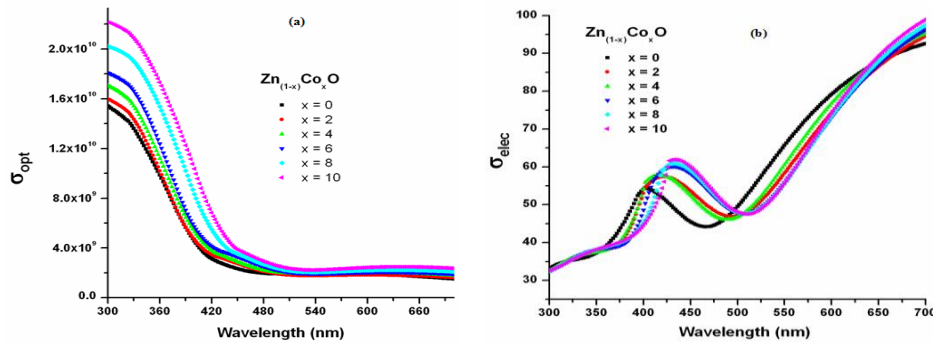


Fig. 9. (a) Optical and (b) electrical conductivity versus the wavelength for $Zn_{1-x}Co_xO$ ($0.0 \leq x \leq 0.10$) films.

From the Fig.9a, the optical conductivity decreases with wavelength, when it is moving from the UV-side to the visible side, until 450 nm and then remains almost constant between 450 nm and 700 nm. It can be explained as follows: Initially, high photoconductivity was observed in the UV-region as the available free charges absorb incident photon energy and it decreases as the energy of the incident photon decreases. The increase of σ_{opt} as result of the increase of Co content could be attributed to the formation structure defects or scattering centers which cause an increase in the optical absorption in the investigated films [4].

From this Fig.9b, the general trend of σ_{elec} is to increase with wavelength, which is also obvious from Eq. (14). The σ_{elec} displays an inverse relationship with Co content except in the wavelength range $450 \text{ nm} > \lambda > 550 \text{ nm}$, it reverses the trend and the σ_{elec} increases with increasing the Co content. The optical conductivity outlines the free carriers in the semiconductor [33].

In scanning electron microscopy, the surface topology and morphology of nano-crystalline $Zn_{1-x}Co_xO$ ($0.0 \leq x \leq 0.10$) thin films have been studied. Figure 5(a&b) shows the SEM images of the $Zn_{1-x}Co_xO$ film. Due to the presence of Co dopants, more impurities are present in ZnO crystals, resulting in more defects and changes in the crystal network, so that the crystallinity of the film is reduced by the reduction of the crystallite size calculated by XRD. The average grain size evaluated from the SEM image is closer than the one calculated from the XRD pattern.

3.2.2. Dielectric constants

The dielectric is more meaningful to the electronic structure of the material and is directly related to the density of states in the restricted band that affects the electromagnetic radiation through which the material passes. This characteristic of the complex dielectric function can be studied, as described below [41]:

$$\varepsilon = \varepsilon_1 + i \varepsilon_2, \quad (15)$$

where ε_1 is the actual part of the dielectric constant related to the slowing of the speed of light in the material. ε_2 is the imaginary part of the dielectric constant, which paves the way for the absorption of energy from the electric field through dipole motion. The same applies to refractive index and extinction, as:

$$\varepsilon_1 = n^2 - k^2 \quad (16)$$

$$\varepsilon_2 = 2nk. \quad (17)$$

The relationship between ε_1 and ε_2 versus wavelength is shown in Figs. 10 (a, b). Figures.10 (a&b) represent the plot of real as well as imaginary parts (ε_1 and ε_2) of dielectric constant versus wavelength, for as-prepared $Zn_{1-x}Co_xO$ ($0.0 \leq x \leq 0.10$) films.

Absorption peaks for ε_1 are shifted to high wavelength with increasing Co content while, the peak intensities increase. The spectral distribution of ε_2 for $Zn_{1-x}Co_xO$ films are shown in Fig.10b. The graph shows absorption peaks shifted to lower energy side was also observed with increase of Co content. It is observed that both the real and imaginary parts of the dielectric constant increases with increase in Co-doping concentration.

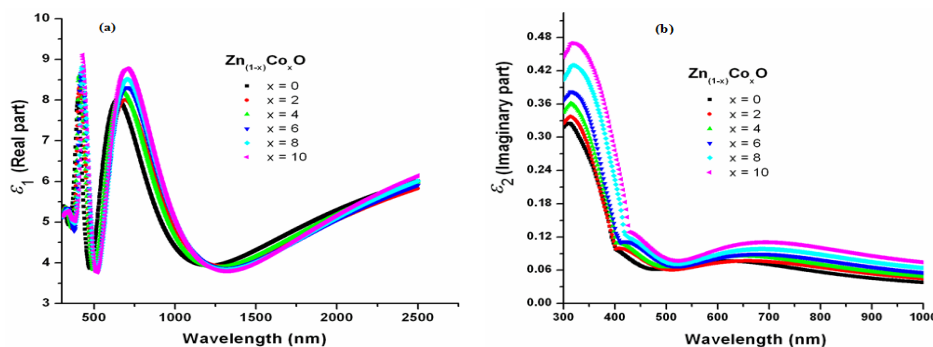


Fig. 10. Spectral behaviors of (a) ε_1 and (b) ε_2 versus λ for $Zn_{1-x}Co_xO$ ($0.0 \leq x \leq 0.10$) films.

3.2.3. Energy loss functions

In semiconductors, in the inelastic scattering process, energy is transferred to or from the topmost atomic layer. Using the dielectric theory system, the spectral response of this inelastic scattering can be defined as the volumetric energy loss function (VELF) and the surface energy loss function (SELF), which are given by the following equations: [42]. In semiconductors, energy

is transferred into or out of the top atomic layer during inelastic scattering. Using the dielectric theory system, the spectral response of this inelastic scattering can be defined as a function of volumetric energy loss (VELF), and the function of surface energy loss (SELF) is given by the following equation [42]:

$$VELF = \frac{\epsilon_2}{\epsilon_1^2 + \epsilon_2^2} \quad (18)$$

$$SELF = \frac{\epsilon_2}{(\epsilon_1 + 1)^2 + \epsilon_2^2} \quad (19)$$

The energy dependence of pure ZnO and treated Zn_{1-x}Co_xO films on the volume and surface energy loss function is shown in Figure 11 (a, b). It can be seen from the figure that the energy loss experienced by free charge carriers when moving across the volume and surface is similar. In addition, it is observed that the surface energy loss is lower than the volumetric energy loss, and as the implantation level increases, both functions increase.

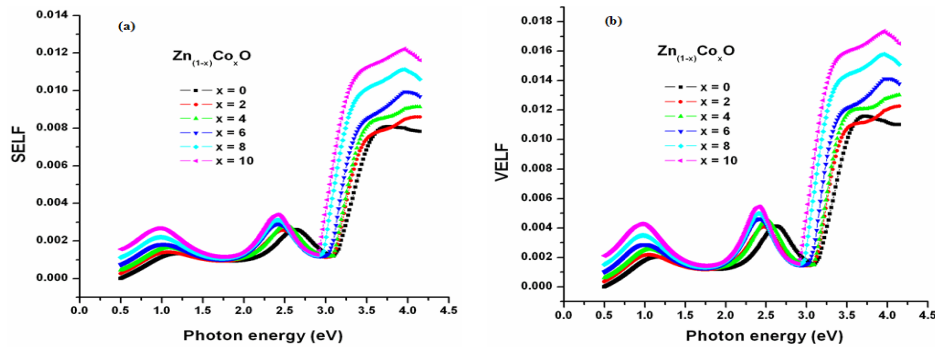


Fig. 11. Variation of (a) surface energy loss function (SELF) and (b) volume energy loss function (VELF) as a function of the photon energy ($h\nu$) for as-prepared Zn_{1-x}Co_xO ($0.0 \leq x \leq 0.10$) films.

3.3. Nonlinear studies of Zn_{1-x}Co_xO ($0.0 \leq x \leq 0.10$) films

Oxide films have high nonlinear optical sensitivity and can provide extensive details of the films, so it is important to understand how light passes through them [36-38]. The convincing relationship between the refractive index nonlinearity of the evaluation film and the light polarization is given by [38]:

$$P = \chi^{(1)}E + P_{nl}, \quad (20a)$$

and

$$P_{nl} = \chi^{(2)}E^2 + \chi^{(3)}E^3, \quad (20b)$$

where P is polarizability, $\chi^{(1)}$ is linear susceptibility, whereas the second and third order nonlinear susceptibilities are designated by $\chi^{(2)}$ and $\chi^{(3)}$, respectively [39].

Moreover, the linear refractive index, $n(\lambda)$ could be written as [40]:

$$n(\lambda) = n_o(\lambda) + n_2(\lambda), \quad (21)$$

where $(E)^2$ is mean square of electric field [41]. Usually, $n_o(\lambda) \gg n_2(\lambda)$, resulting in $n(\lambda) = n_o(\lambda)$. The $\chi^{(1)}$ is given by the expression [38,39]:

$$\chi^{(1)} = \frac{n^2 - 1}{4\pi}, \quad (22)$$

while the third order nonlinear susceptibility $\chi^{(3)}$ is related to $\chi^{(1)}$ by [38,39]:

$$\chi^{(3)} = A. [\chi^{(1)}]^4, \quad (23)$$

and so,

$$\chi^{(3)} = \frac{A}{(4\pi)^4} (n_o^2 - 1)^4, \quad (24)$$

where $A=1.7 \times 10^{-10}$ esu is a constant [42, 43]. The nonlinear refractive index, $n^{(2)}$ has the simple form [44]:

$$n^{(2)} = \frac{12\pi\chi^{(3)}}{n_o}. \quad (25)$$

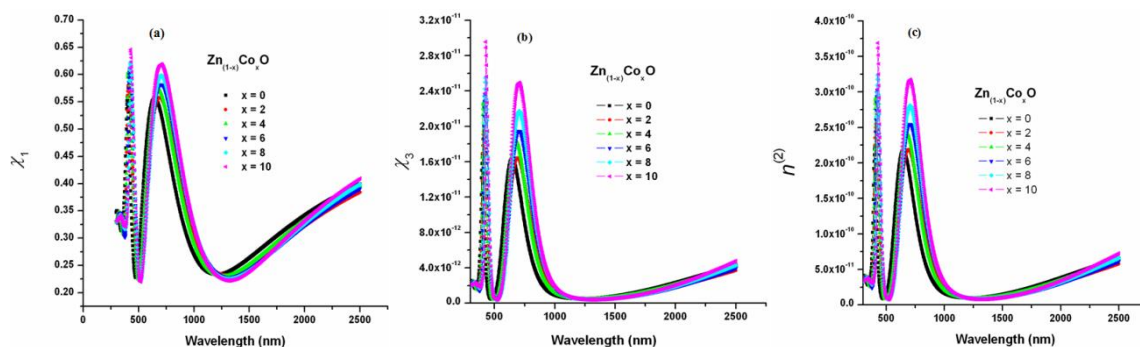


Fig. 12. Spectral behaviors of (a) linear optical susceptibility, $\chi^{(1)}$, (b) nonlinear optical susceptibility, $\chi^{(3)}$, and (c) nonlinear refractive index, $n^{(2)}$, versus λ for $Zn_{1-x}Co_xO$ ($0.0 \leq x \leq 0.10$) films.

Figures 12(a&b) represent the plots of $\chi^{(1)}$ and $\chi^{(3)}$ with respect to the wavelength for the $Zn_{1-x}Co_xO$ thin films. The graph of $\chi^{(1)}$ strongly resembles that of ϵ_1 with a slight shift in the wavelength indicating a strong dependency between the two. The $\chi^{(1)}$ values are found to be in the range of 0.22 to 0.65. From this figure, both $\chi^{(1)}$ and $\chi^{(3)}$ follow the similar trend in intensity variation against the wavelength for various Co content of $Zn_{1-x}Co_xO$ thin films. Fig.12(c) portrays the plot of nonlinear refractive index ($n^{(2)}$) with respect to wavelength for $Zn_{1-x}Co_xO$ thin films. It is a key quantity of the material which offers significant data regarding the light gathering capacity of the film. The graph exactly resembles that of $\chi^{(3)}$ and reveals a very strong reliance of $n^{(2)}$ on $\chi^{(3)}$.

4. Magnetic measurements

Magnetic measurements were performed by a Vibrating Sample Magnetometer (VSM). At room temperature (300 K), along the $Zn_{1-x}Co_xO$ ($0.0 \leq x \leq 0.10$) film plane, the dependence of the magnetization on the magnetic field range from -20 to 20 kOe is shown in Figure 13. These results are the removal of the glass substrate Plotted after the influence, showing the diamagnetic contribution.

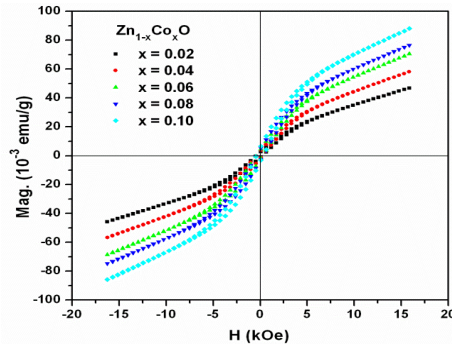


Fig. 13. Room temperature Magnetic hysteresis loops for $Zn_{1-x}Co_xO$ ($0.0 \leq x \leq 0.10$) thin films.

The black curve shown in Fig. 14(a) represents undoped ZnO, revealing the diamagnetic behavior (negative susceptibility) associated with ferromagnetic rings with visible coercivity and saturation magnetization. On the other hand, Fig. 14(b) shows the paramagnetic behavior of CoO. In addition, the addition of Co as a dopant in the $Zn_{1-x}Co_xO$ nanocrystalline film helps to enhance the magnetic moment, as shown in figure 13 (color hysteresis M-H curve), as the percentage of Co increases, the saturation magnetization (M_s) increases. After Co doping, the origin of ferromagnetism, which is now called dilute magnetic semiconductor, will be through another mechanism (bound magnetopolaron (BMP) [27, 28], or carrier-induced Ruderman-Kittel-Kasuya-Yosida exchange Interaction) to explain, (RKKY) [29, 30]). The increased ferromagnetism of Co doping shown in figure 8 can be explained by the dual exchange mechanism (RKKY), which uses carrier-induced ferromagnetism [31].

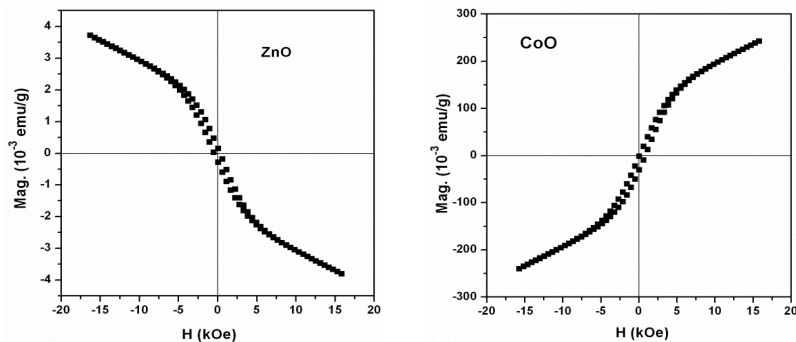


Fig. 14. (a&b): Room temperature Magnetic hysteresis loops (a) for pure ZnO thin film and (b) for CoO thin film.

5. Conclusion

$Zn_{1-x}Co_xO$ ($0 \leq x \leq 0.10$) thin film is prepared by ball milling method. All films show a hexagonal wurtzite crystal structure, and the crystallite size is reduced. The optical constants of the $Zn_{1-x}Co_xO$ film are extracted in the range of 300-2500 by spectrophotometer. The optical constants (n , k) and film thickness d are determined according to $k-k$ method. The refractive index increases with the increase of Co concentration, while the energy gap behavior shows that the content of the $Zn_{1-x}Co_xO$ film decreases with the increase of Co. The decrease of E_g^{opt} may be due to the decrease of crystal size and heat of atomization. Undoped ZnO shows diamagnetic behavior (negative permittivity) associated with ferromagnetic rings with visible coercivity and saturation magnetization. The dependence of the magnetization on the magnetic field illustrates the ferromagnetic behavior of Co-doped ZnO.

Acknowledgements

The authors thank King Khalid University, Ministry of Education, Kingdom of Saudi Arabia for funding this research through a grant: (RCAMS/KKU/013/20) under research center for advanced material science

References

- [1] T. Fukumura, Y. Yamada, H. Toyosaki, T. Hasegawa, H. Koinuma et al., *Appl. Surf. Sci.* **223**, 62 (2004).
- [2] U. Uzgür, I. Alivov, C. Liu, A. Teke, M. Reshchikov, *Appl. Phys. Rev* **98**, 041301 (2005).
- [3] N. H. Nickel, E. Terukov, Zinc Oxide-A Material for Micro-and Optoelectronic Applications: Proceedings of the NATO Advanced Research Workshop on Zinc Oxide as a Material for Micro-and Optoelectronic Applications, held in St. Petersburg, Russia, from 23 to 25 June 2004, Springer Science & Business Media 2006.
- [4] N. H. Hong, J. Sakai, N. Poirot, V. Brizé, *Phys. Rev. B* **73**, 132404 (2006).
- [5] H. Ohno, (1998) *Science* **951**, 281 (1998).
- [6] H. Ohno, H. Munekata, T. Penney, S. von Molnar, L. L. Chang, *Phys. Rev. Lett.* **68**, 2664 (1992).
- [7] G. A. Prinz, *Science* **1660**, 282 (1998).
- [8] H. Ohno, *Science* **281**, 951 (1998).
- [9] J. K. Furdyna, J. Kossut, *Diluted Magnetic Semiconductors*, Academic Press, 1988.
- [10] R. N. Aljawfi, S. Mollah, J. Magn. Mater. **323**, 3126 (2011).
- [11] E. R. Shaaban, I. Kansal, S. Mohamed, J. M. Ferreira, *Physica B: Condensed matter* **404**, 3571 (2009).
- [12] H. T. Ng, J. Han, T. Yamada, P. Nguyen, Y. P. Chen, M. Meyyappan, *Nano Lett.* **4**, 1247 (2004).
- [13] J. C. Johnson, H. Yan, P. Yang, R. J. Saykally, *The journal of physical chemistry B* **107**, 8816 (2003).
- [14] J. Cao, J. Wu, *Mater. Sci. Eng. R* **71**, 35 (2011).
- [15] E. R. Shaaban, M. N. Abd-el Salam, M. Mohamed, M. A. Abdel-Rahim, A. Y. Abdel-Latief, *Journal of Materials Science: Materials in Electronics* **28**, 13379 (2017).
- [16] N. S. Norberg, K. R. Kittilstved, J. E. Amonette, R. K. Kukkadapu, D. A. Schwartz, D. R. Gamelin, *J. Am. Chem. Soc.* **126**, 9387 (2004).
- [17] E. R. Shaaban, M. Y. Hassaan, M. G. Moustafa, A. Qasem, G. A. M. Ali, *Optik* **186**, 275 (2019)
- [18] B. D. Cullity, *Elements of X-ray diffraction*. 2nd ed. London: Addition-Weasley; 1978.
- [19] J. I. Langford, A. J. C. Wilson, *J. Appl. Cryst.* **11**, 102 (1978).
- [20] J. Sivasankar, P. Mallikarjana, M. Rigana Begam, N. Madhusudhana Rao, S. Kaleemulla, J. Subrahmanyam, *Journal of Materials Science: Materials in Electronics* **27**, 2300 (2016).
- [21] D. Prakash, A. M. Aboraia, M. El-Hagary, E. R. Shaaban, K. D. Verma, *Ceramics International* **42** (2), 2676 (2016).
- [22] H. Fujiwara, *Spectroscopic Ellipsometry: Principles and Applications*. 2007: Wiley.
- [23] S. R. Elliott, *The Physics and Chemistry of Solids*, Wiley, Chichester, 2000.
- [24] A. Sundaresan, R. Bhargavi, N. Rangarajan, U. Siddesh, C. Rao, *Phys. Rev. B* **74**, 161306 (2006).
- [25] Q. Wang, Q. Sun, G. Chen, Y. Kawazoe, P. Jena, *Phys. Rev. B* **77**, 205411 (2008).
- [26] N. H. Hong, J. Sakai, V. Brizé, *J. Phys.: Condens. Matter* **19**, 036219 (2007).
- [27] N. H. Hong, J. Sakai, N. T. Huong, N. Poirot, A. Ruyter, *Phys. Rev. B* **72**, 045336 (2005).
- [28] M. Emam-Ismail, M. El-Hagary, E. R. Shaaban, S. Althoyaib, *Journal of alloys and compounds* **529**, 113 (2012).
- [29] S. Ramachandran, J. Narayan, J. Prater, *Appl. Phys. Lett.* **88**, 242503 (2006).
- [30] S. Koshihara, A. Oiwa, M. Hirasawa, S. Katsumoto, Y. Iye, C. Urano, H. Takagi,

- H. Munekata, *Phys. Rev. Lett.* **78**, (46171997).
- [31] E. R. Shaaban, M. M. Mahasen, M. M. Soraya, E. S. Yousef, S. A. Mahmoud, G. A. Ali, H. A. Elshaikh, *J. Am. Ceram. Soc.* **102**, 4067 (2019).
- [32] V. Gandhi, R. Ganesan, H. H. Abdulrahman Syedahamed, M. Thaiyan, *J. Phys. Chem. C* **118**, 9715 (2014).